Fluid Dynamics &
Materials Processing

Tech Science Press

http://doi.org/10.32604/fdmp.2026.083363

ARTICLE

Swirl-Induced Flow Instabilities and Heat Transfer Enhancement in Vertical Falling Films at High Reynolds Numbers

Lishuang Zheng[1,*] and Fengjun Chen[2]

[1]School of Mechanical Engineering, Henan Institute of Technology, Xinxiang, China
[2]School of Materials Science and Engineering, Henan Institute of Technology, Xinxiang, China
*Corresponding Author: Lishuang Zheng. Email: lishuangz2026@163.com

Received: 06 April 2026; Accepted: 30 June 2026; Published: 31 July 2026

ABSTRACT: A computational fluid dynamic (CFD) numerical framework is established in this article to comprehensively uncover the flow evolution laws and gas-liquid phase-change heat transfer mechanisms of vertical falling film with high Reynolds numbers (*Re*). Systematic numerical analysis are carried out to characterize the liquid film spatial distribution, flow velocity field, internal turbulent vortex structures and comprehensive heat transfer behaviors. The swirl-induced coherent structures are identified using velocity vectors and vortex-detection criteria, and the influences of swirl angle, channel width, and platform height on film thickness distribution and thermal performance are examined. Model validation is performed through comparison with published numerical and experimental data, showing good agreement. The results indicate that, under high Re conditions, swirling motion significantly disrupts the liquid film and intensifies interfacial turbulence, thereby enhancing heat transfer. The inlet region exhibits the highest thermal performance, driven by strong vortex activity. Increasing the swirl angle leads to a reduction in liquid film thickness and an overall enhancement of heat transfer. However, turbulent kinetic energy and dissipation rate exhibit nonlinear responses to changes in swirl angle. An optimal configuration is identified at a swirl angle of 60°, where the average film thickness is approximately 4.03 mm and interfacial fluctuations remain most stable. In addition, a coupled optimal range is observed for channel width and platform height, highlighting their combined influence on flow stability and thermal efficiency. The underlying two-phase transport mechanisms are interpreted in terms of vortex dynamics and energy transfer processes. Based on the simulation results, a heat transfer correlation valid for high Re conditions is developed. The maximum heat transfer coefficient reaches approximately 700 $W/m^2 \cdot K$. Furthermore, fitting of the dimensionless heat transfer coefficient (h^+) demonstrates excellent predictive capability for heat transfer trends in gas–liquid two-phase internal flows, with a coefficient of determination (R^2) of 0.999.

KEYWORDS: Swirl falling film; fluid dynamic; liquid film thickness; turbulent flow; phase change heat transfer; HTC

1 Introduction

Vertical falling film inside tube is widely used in the chemical industry, prior research [1–3] highlights that the above phenomenon is highly conspicuous for falling film hydrodynamics and gas-liquid heat transfer under low Reynolds number (*Re*) operating conditions. The liquid film develops fully laminar flow as $Re \leq 30$, which is characterized by slow streamwise velocity and negligible surface wave fluctuationss. When $30 < Re \leq 2000$, the liquid film flow is turbulent laminar flow. Moreover, the liquid film exhibits stronger surface oscillation. Driven by the liquid surface and gravitational pull, capillary undulations and gravity waves appear on the film exterior. When *Re* is no less than 2000, turbulent flow replaces laminar flow on liquid film surface, the film thickness rises, and this thickening effect is amplified with the continuous increase of *Re*. The liquid film will form droplets due to excessive flow velocity and detach from the wall [4].

Two primary research branches have been formed for vertical falling film hydrodynamics in vertical pipes according to liquid *Re* magnitudes. Works under low *Re* conditions prioritize analyzing flow evolution rules, surface wave morphologies and interphase contact features between gas and liquid [5–9]. For high *Re* operating states, researchers mainly explore variables that trigger film collapse and the interference generated by gas phase oscillatory motion [10–14]. Some researchers have studied the effects of surface tension, structural dimensions, and gas-liquid counter-flow, on falling film fluctuations [15–19]. Vasques et al. [20] compared the disturbance wave parameters and flow direction in vertical annular gas-liquid flow in tube. Aktershev and Alekseenko [21] have developed a new model for long wave disturbances in descending liquid films. Based on the boundary layer method, the velocity is expanded into the linearly independent fundamental function (harmonic) system that satisfies the boundary conditions. To reveal the stability evolution rule of nonlinear interfacial waves, linear theoretical analysis and numerical calculation models are adopted for comprehensive research.

Heat exchange between gaseous and liquid phases can be realized by utilizing falling liquid layers along tube inner walls. Thanks to the remarkable thermal exchange efficiency of this flow pattern, high-temperature syngas can be sufficiently cooled and humidified. Plenty of academic papers have explored novel structural designs to intensify two-phase heat transfer inside vertical tubular falling film devices [22,23]. Apart from that, other scholars analyze the core factors dominating the coupled heat and mass transfer accompanied by phase change during gas-liquid direct contact in pipe channels. Including evaporation temperature, airflow velocity, air counter-flow, liquid film velocity, vapor partial pressure [24–28]. Zeng et al. [29] studied swirl vertical falling film flow, and the research demonstrated that the velocity distribution of swirling flow is significantly different from that of vertical flow, with tangential velocity playing the dominant role. Jin et al. [30] further investigated the influence of hydrocyclone geometric parameters on the spiral liquid film spatio-temporal evolution. Numerical calculation findings reveal that lowering the pitch size of the hydrocyclone structure effectively eliminates asymmetric defects and achieves more symmetrical liquid film spreading. Wan [31] conducted numerical simulations of the fluid mechanics and heat transfer performance of elliptical tube membranes using Volume of Fluid (VOF), and studied the effects of heating conditions, fluid medium, and inlet temperature on liquid film thickness and HTC. Relevant laboratory measurements documented in reference [32] characterize the thermal transfer capacity and dirt deposition properties of water within sintered porous stainless steel tubes.

In the research on enhancing heat transfer in gas-liquid two-phase flow, the main focus is on the pipeline structures modification, including cross corrugated channels in plate heat exchangers [33] and new liquid distributors [34]. Kumar et al. [35] conducted experimental research on flow boiling inside tubes, obtaining spatial wall temperature distribution, local heat transfer coefficient, and pressure fluctuations. Zhao et al. [36] studied the specific effects of liquid flow rate, distribution height, bundle spacing, and arrangement on the vertical flow and heat transfer performance of liquid films. Cao et al. [37] studied the thermal characteristics of the vertical annular corrugated tube with dual air/water capabilities. Dong et al. [38] used the single-phase multi-component condensation model, combined with equations describing flow and heat transfer, to study the heat transfer characteristics of steam air flow in the sinusoidal vertical corrugated tube under different inlet velocities, air mass fractions, and wall subcooling. The two-phase flow simulation work recorded in reference [39] utilizes the VOF algorithm with adjustable steam mass flow ratios, aiming to characterize the heat transfer boosting capabolity of fin componernts within pipe passage.

In the previous studies, there are few researches on the breakup and turbulence effects caused by the vertical liquid film flow process. The most vigorous gas-liquid interaction occurs at the front inlet zone of the pipe during two-phase flow with heat transfer. Uneven distribution of liquid film thickness can lead to uneven heat transfer between gas and liquid, resulting in wall drying. A cyclone vertical falling film can effectively solve the problem of liquid film thickness uneven distribution. This article is based on this research point and uses Computational Fluid Dynamics (CFD) to establish the swirling falling film device. To obtain the optimum structural parameters of the device, systematic investigations are performed to quantify the impacts of varied swirl angles, platform heights and slit sizes on the liquid layer thickness layout, flow field distribution and turbulent fluctuation strength. Research the influence of liquid film *Re*, gas temperature, and gas phase *Re* on the heat transfer process, and compare it with the opposed vertical falling film heat transfer process. The main purpose of this research is to investigate the factors that affect the cyclone falling film and study the gas-liquid two-phase heat transfer process in the inlet section of the cyclone falling film. The main contribution of this study is to provide new empirical correlations for the uniform flow and heat transfer of liquid films in practical applications.

The innovations of this research are as follows:

1. This research systematically investigates the gas-liquid two-phase flow and heat transfer characteristics of a swirling vertical falling film under high *Re* conditions, filling the research gap that most existing studies focus on low *Re* and lack in-depth flow-thermal coupling analysis at high *Re*.
2. Based on turbulent criterion vortex identification and velocity vector field visualization, explain the heat transfer enhancement mechanism of falling film at high *Re* from the perspective of vortex dynamics.
3. The correlations of the heat transfer coefficient suitable for high *Re* swirling falling film are established, and the effects of liquid film *Re* and temperature are clarified.

2 Swirl Physics Model and Verification

2.1 Swirl Physics Model

Fig. 1 illustrates the physical model of cyclone falling film system. After the cooling water enters the annular cooling component, stable homogeneous liquid film is formed when the fluid flows across the narrow gap. Heat exchange takes place in the gas-liquid two-phase flow fleid: gas medium enters the pipe from the intake port and exchanges heat with the liquid film by direct contact, thereby inducing vaporization and phase change of liquid film. Complete structural and operational parameter data are recorded in Table 1.

Table 1: Structural parameters of swirling vertical falling film device.

Structure Name	Diameter/mm	Length/mm	Width/mm	Angle/°
Liquid inlet	19	/	/	45
Slot	/	/	3	/
Outlet	146	/	/	/
Air inlet	120	/	/	/
Tube	146	500	/	/
Scrubbing cooling ring	/	43	/	/

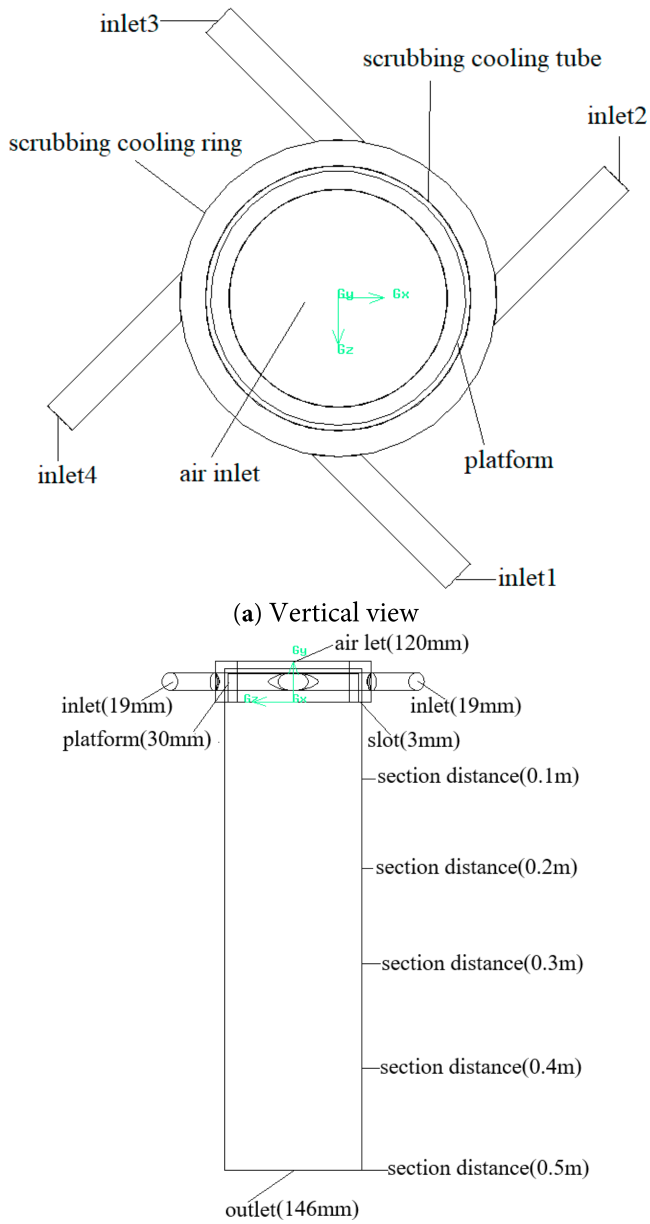

(**a**) Vertical view

(**b**) Front view

Figure 1: Swirl falling film model. (**a**) Vertical view, (**b**) Front view.

2.2 Model Boundary Condition Setting and Assumptions

For the hydrodynamic simulation of gravity-driven liquid film, air and water are designated as the two-phase working medium. The VOF-based miltiphase flow numerical framework is established, and all numerical solving processes adopt double-precision transient calculation modes. Initialize the model and control that there is only air present at the initial time. Add the air-water surface tension model, and set the surface tension between gas-liquid phase to constant of 0.07305 N/m. Gas-liquid two-phase inlet boundary is velocity inlet, set the outlet as pressure outlet. 2.5×10^{-5} s is selected as the iteration time step for transient solving. In unsteady numerical simulations, the Courant number is directly determined by time step size, excessive step values will push up the Courant number and cause a sharp rise in computing consumption [7]. On the basis of the research framework presented in reference [7], the swirling device model applies the following computational assumptions:

(1) No time-dependent variation exists in the liquid inlet flow velocity.
(2) Under standard atmospheric pressure and ambient temperature conditions, all physical characteristic parameters of gas and liquid phases are unchanged.

The wall is set to no velocity slip boundary condition, and the expression for the liquid film Re is as follows [40]:

$$Re = \frac{4I}{\mu_l} \tag{1}$$

$$I = \frac{m_l}{\pi D} \tag{2}$$

Re is liquid film Reynolds number, I is unit wet weekly mass flow rate, kg/(m·s), μ_l is liquid film dynamic viscosity, Pa·s, m_l is mass flow rate, kg/s, D is liquid film inlet diameter, mm.

According to reference [7], RNG k-ε model is most suitable for liquid film turbulent flow inside tube. The reason is that compared to the SST k-ω model, RNG k-ε has lower requirements for the model grid, with y+ around 30. For grids with larger y+, RNG k-ε can be modified for high strain rates, large curvatures, and separated flows, which can better handle the liquid film spreading and fluctuation on complex walls. The SST k-ω model has high requirements for grid y+, and y+ around 30 can lead to severe distortion of wall shear stress and heat transfer calculation results. So choose the RNG k-ε model in this research [7,40]. The continuity equation and mixing density of gas-liquid two-phase flow are as follows [40]:

$$\frac{\partial \rho}{\partial t} + \nabla \cdot (\rho u) = 0 \tag{3}$$

$$\rho = \alpha_l \rho_l + \alpha_g \rho_g \tag{4}$$

ρ is mixed density, kg/m^3, u is velocity, m/s, α_l is liquid phase volume fraction, ρ_l is liquid phase density, kg/m^3, α_g is gas phase volume fraction, ρ_g is gas phase density, kg/m^3.

The transport equation for the liquid phase volume fraction is as follows:

$$\frac{\partial \alpha_l}{\partial t} + u\nabla \alpha_l = -\frac{m_{lv}}{\rho_l} \tag{5}$$

m_{lv} is the evaporation mass transfer rate of liquid phase to gas phase per unit volume, kg/m^3·s.

The mass transfer rate equation under evaporation conditions ($T_l > T_{sat}$) is as follows, where T_l is the liquid film temperature, K, and T_{sat} is the saturation temperature at operating pressure, K.

$$m_{lv} = C\alpha_l \rho_l \frac{T_l - T_{sat}}{T_{sat}} \tag{6}$$

C is the coefficient of evaporation, 0.1~0.3.

The momentum equation and energy equation of the calculation model are as follows:

$$\frac{\partial \rho \vec{u}}{\partial t} + \frac{\partial(\rho \vec{u}\vec{u})}{\partial x_j} = -\frac{\partial P}{\partial x_i} + \frac{\partial}{\partial x_j}[\mu(\frac{\partial \vec{u}_i}{\partial x_j} + \frac{\partial \vec{u}_j}{\partial x_i})] + \frac{\partial}{x_j}(-\rho \vec{u}_i \vec{u}_j) + \rho g + F \tag{7}$$

$$F = \sigma k_{g-s} \nabla \alpha_l$$

$$\mu = \alpha_l \mu_l + \alpha_g \mu_g$$

$$\frac{\partial(\rho c_p T)}{\partial t} + \nabla \cdot (\rho \vec{u} c_p T) = \nabla \cdot (\lambda \nabla T) + \mu(\frac{\partial u_i}{\partial x_j} + \frac{\partial u_j}{\partial x_i})\frac{\partial u_i}{\partial x_j} + S_{h,evap} \tag{8}$$

$$\lambda = \alpha_l \lambda_l + \alpha_g \lambda_g$$

$$S_{h,evap} = -m_{lv} h_{lv}$$

$$C_p = \frac{\alpha_l C_l \rho_l + \alpha_g C_g \rho_g}{\rho}$$

P is pressure, Pa, μ is dynamic viscosity, Pa·s, μ_l is liquid film dynamic viscosity, Pa·s, μ_g is gas dynamic viscosity, Pa·s, g is acceleration due to gravity, m/s^2, F is body force, N, σ is surface tension, 0.07305, N/m, k_{g-s} is Local curvature of gas-liquid interface, c_p is specific heat capacity, J/kg·K, T is temperature, K, λ is thermal conductivity, W/m·K, λ_l is liquid film thermal conductivity, W/m·K, λ_g is gas thermal conductivity, W/m·K, $S_{h,evap}$ is evaporative phase transition source term, h_{lv} is latent heat of vaporization of water, J/kg.

2.3 Boundary Conditions

Constraints applied to the two-phase separating surface consist of kinematic boundary relations and heat transfer boundary equations. The mass flux crossing the interphase surface is dominated by the normal velocity of gas and liquid at the contact boundary. The boundary conditions for motion are as follows:

$$m = \rho_l(u_l - u_i) \cdot \vec{n} = \rho_g(u_g - u_i) \cdot \vec{n} \tag{9}$$

m is the cold mass flux, kg/s. Eq. (9) represents the mass conservation boundary condition at the gas-liquid interface. When the flow inside the tube boils, $m > 0$, quality enters the gas phase from the liquid phase. The opposite is true for flow condensation.

Assuming the interface is in the local thermodynamic equilibrium state, the temperature on both sides of the interface is continuous, and temperature is equal to the saturation temperature corresponding to the working pressure. The heat transfer boundary conditions are as follows:

$$T_l = T_g = T_{sat} \tag{10}$$

$$\lambda_g \frac{\partial T_g}{\partial x} - \lambda_l \frac{\partial T_l}{\partial x} = m_{lv} h_{lv} \tag{11}$$

λ_g is gas phase thermal conductivity, W/m·K, λ_l is liquid phase thermal conductivity, W/m·K, h_{lv} latent heat of vaporization, J/kg. Under the condition of evaporation phase transition inside the tube, heat is mainly transferred from the gas phase to the liquid phase. The component boundary conditions at the gas-liquid interface are as follows:

$$\rho_g D_g \frac{\partial Y}{\partial x} = m_{lv}(1 - Y_i) \tag{12}$$

D_g is the gas phase diffusion coefficient, Y is the vapor mass fraction, Y_i is the neat volume fraction at the interface.

Boundary relations corresponding to the gas-liquid contact interface are defined by Eqs (9)–(12). Integrating these interphase constraints, wall boundary treatments and inlet-outlet boundary specifications yields the full mathematical framework for this numerical research.

2.4 Grid and Model Validation

Grid partitioning and numerical validation of vertical swirling falling film geometric model are implemented in the initial stage to further reveal the liquid film flow patterns inside tube. The mesh is divided into unstructured regular undergoes encryption. The reason for this encryption is the swirling vertical falling film represents the complex model, and the swirling process requires precise calculation, thus necessitating the refinement of model mesh. After grid refinement, the grid y+ is basically around 30, and RNG k-ε is selected as the turbulence model. The PISO (Pressure Implicit with Splitting of Operators) algorithm is selected for pressure–velocity decoupling, which is suitable for transient unsteady multiphase flow with strong interface fluctuation. Compared with the steady-state SIMPLE algorithm, PISO contains multiple pressure correction steps within single time step, which effectively suppresses numerical oscillation of liquid film thickness and velocity field under high Re swirling conditions. Turbulent kinetic energy, dissipation rate, and momentum parameters are all presented in the second-order upwind format. The grid generation and independence verification for the swirling vertical falling film model are shown in Fig. 2. The criteria for grid independence validation are based on liquid film thickness values at the cross-sections of the inlet section, fully developed section, and liquid film outlet section.

Fig. 2 illustrates the mesh division and independence verification for the swirling vertical falling film flow model. Fig. 2a shows the model mesh division, with the fluid domain undergoing mesh refinement. Fig. 2b reflects the grid independence validation. Select axial liquid film thickness at $Re = 3.63 \times 10^4$ in the verification. The plotted data reveals a positive correlation between mesh element quantity and liquid film thickness. When the total mesh scale reaches 6.6×10^5, the liquid layer thickness variation tends to vanish. Further mesh refinement cannot change the distribution characteristics of wall liquid film, so the mesh scale of 6.6×10^5 is determined as the optimal grid division.

To prove that the adopted simulation scheme is practicable and deviation free, benchmark comparisons against experimental measurements are implemented based on the test scheme recorded in reference [40]. The test cooling tube possesses a 1000 mm overall length, 138 mm internal diameter, 21 mm inner diameter of the liquid feeding port, and 3 mm slot width. The geometric model is built strictly following the physical dimensions of the test apparatus, and the same computational framework introduced in literature [40] is applied throughout the simulation process—using the RNG k-ε turbulence model, setting the surface tension model parameter to 0.07305 N/m, and enabling the gravity option—the pressure-velocity coupling is solved with PISO to accurately compute the wall liquid film parameters. All governing quantities including momentum, phase volume fraction, turbulent kinetic energy and its dissipation parameter are solved with second-order upwind discretization. The liquid film thickness at the cross-section is selected for comparative validation, and the deviation from the experimental data is calculated. The mathematical model, grid division and comparative validation are shown in Fig. 3.

Fig. 3 plots the deviation comparison between numerically predicted values and real experimental readings. As can be seen from the data deviation in Fig. 3, the maximum deviation between the calculated data and the actual experimental measurements does not exceed 18%, remaining mostly within 15%. In practical engineering applications, deviations between simulated calculations and experimental data within

20% are within the acceptable range. It can be concluded that the simulation algorithm delivers reliable prediction precision and can be applied effectively. Hence, this numerical solving framework is selected for all subsequent calculations in this work.

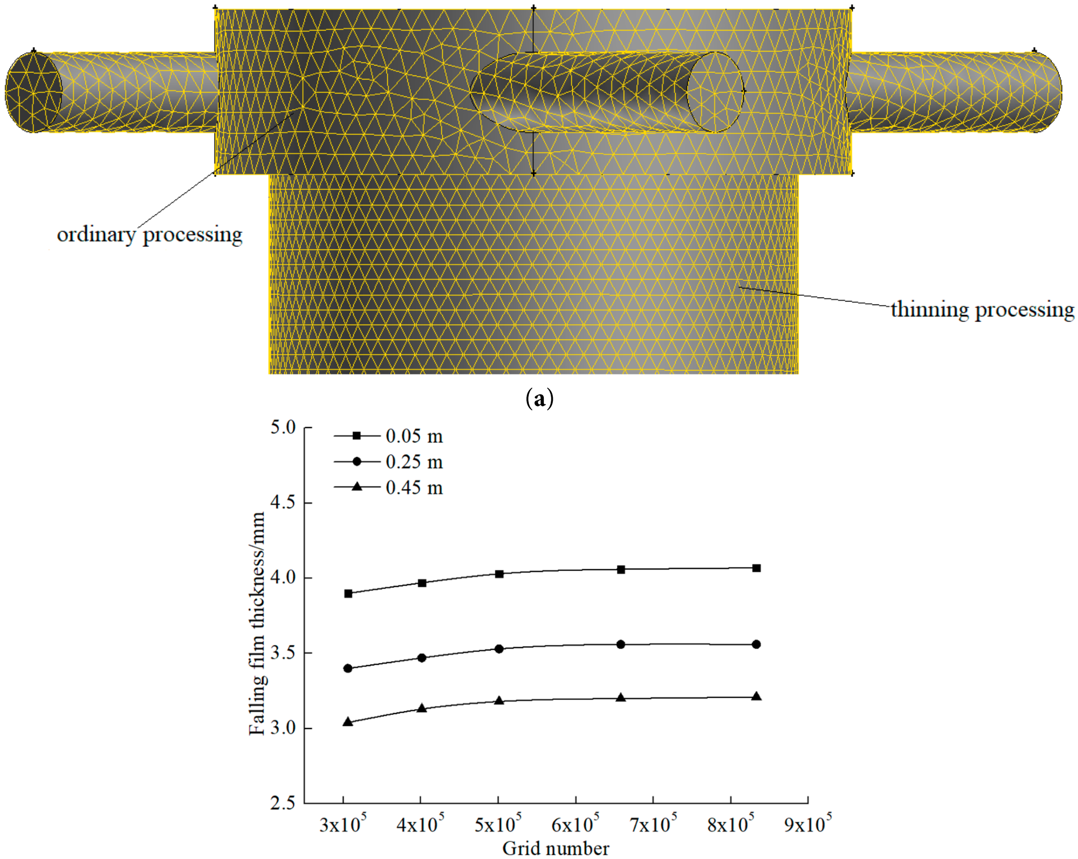

Figure 2: Model grid division and verification. (**a**) Model grid division; (**b**) Grid independent verification.

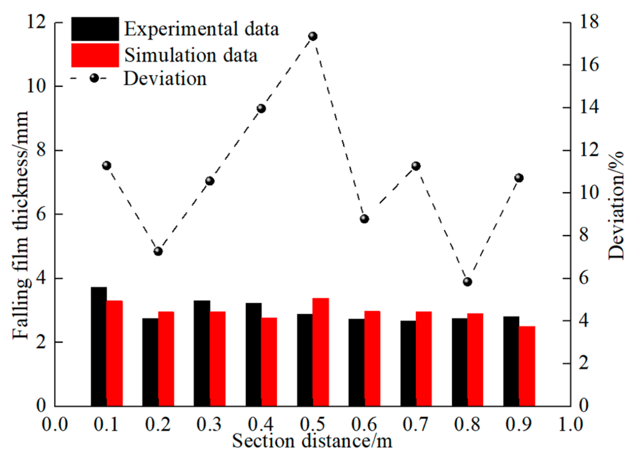

Figure 3: Verification of simulation calculation method.

3 Swirling Vertical Falling Film

3.1 Impacts of Swirl Angle on the Hydrodynamic Behaviors of Falling Liquid Film

Conventional counter-flow vertical falling film devices allow the working liquid to be uniformly distributed by the scrubbing cooling structure and subsequently descend vertically along the slit channel. Conventional counter-flow vertical falling devices allow the working liquid to be uniformly distributed by the scrubbing cooling structure. Different from conventional structures, the swirling falling film configuration features an inclined inlet layout, which induces circumferential liquid motion within the cooling ring prior to the vertical downward flow along the cooling pipeline. It follows that the distribution morphology of falling liquid film is highly dependent on the swirl angle. Under a constant inlet liquid Re of 3.63×10^4, numerical simulations are performed for swirl angles ranging from 0°~75°, and the results are summarized in Fig. 4.

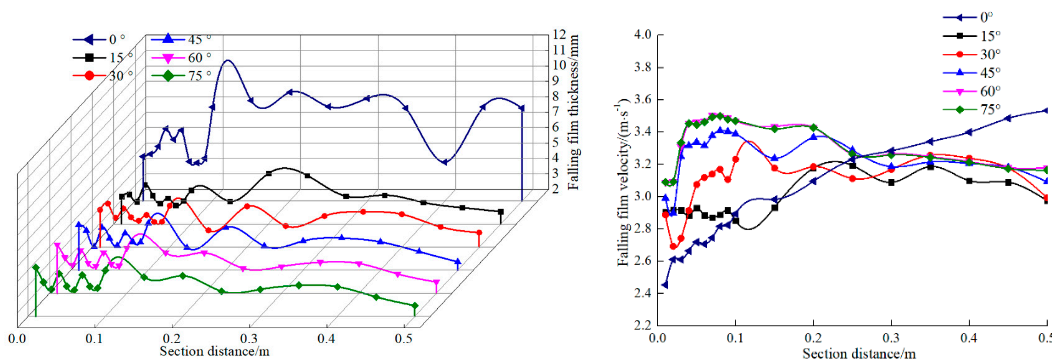

Figure 4: Falling film thickness and velocity of swirl angle. (**a**) Falling film thickness; (**b**) Falling film velocity.

Fig. 4 illustrates the impacts of different swirl angles on the fluctuating behaviors of the liquid layer. The cross-sectional distance on the horizontal axis in the figure is the axial distance inside the tube. From Fig. 4a,b, the liquid film thickness increases in the inlet section (0~0.1 m). When the swirl angle is 0°, the increase in liquid film thickness in inlet section is the largest, while the increase in liquid film thickness at other swirl angles is relatively small. Such a results originates from the flow condition at 0°swirl angle. Since all liquid film momentum components point axially, the fluid gathers quickly at the inlet and brings about an obvious increase in liquid film thickness. As the swirl angle increases, some axial momentum is converted into tangential and radial components, promoting the liquid film diffusion in the circumferential direction, thereby suppressing the sharp increase in the inlet section thickness. As the increment of axial velocity diminishes, the thickening tendency of liquid film is weakened. The liquid layer thickness undergoes sustained fluctuation in the fully developed section (0.1~0.4 m), and then decreases steadily approaching the outlet area (0.4~0.5 m). Elevated swirl angle leads to a continuous rise of liquid film velocity near the inlet. When the swirl angle is increased up to 60°, the liquid film velocity barely changes. Therefore, 60° can be regraded as the critical value to realize effective acceleration of liquid film, under which the average liquid film thickness is 4.03 mm.

As shown in the liquid film thickness distribution in Fig. 4, during the vertical swirling falling film process, the film exhibits significant fluctuations in the inlet section. As the vertical position extends downward, the falling liquid film gains higher flow velocity, and its thickness decreases correspondingly. During the flow process, the liquid film is subjected to the effects of gravity and wall shear stress, which makes it difficult for the liquid film to adhere well to the wall and flow, resulting in turbulent instability on the liquid film surface. The swirl angle not only influences the liquid film thickness distribution but also affects the turbulent effects during the film flow. The turbulent motion of the wall-attached liquid film plays a decisive role in the two-phase heat exchange occurring inside the pipeline. The swirl angle also affects liquid film flow velocity. The vortex structure generated by the liquid film on the tube wall is analyzed using velocity vector figures. Swirl angles of 0°, 45°, 60° are selected to analyze the vortex structure inside the tube. The specific velocity vector figures are shown in Figs. 5 and 6.

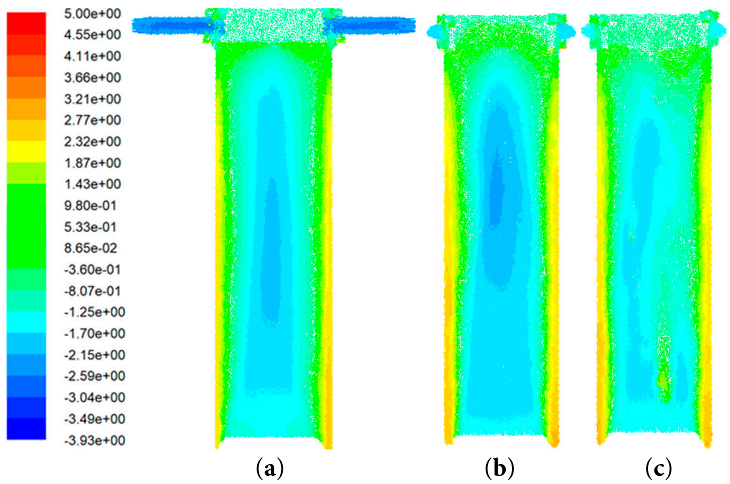

Figure 5: Cross-sectional velocity vector. (**a**) 0°; (**b**) 45°; (**c**) 60°.

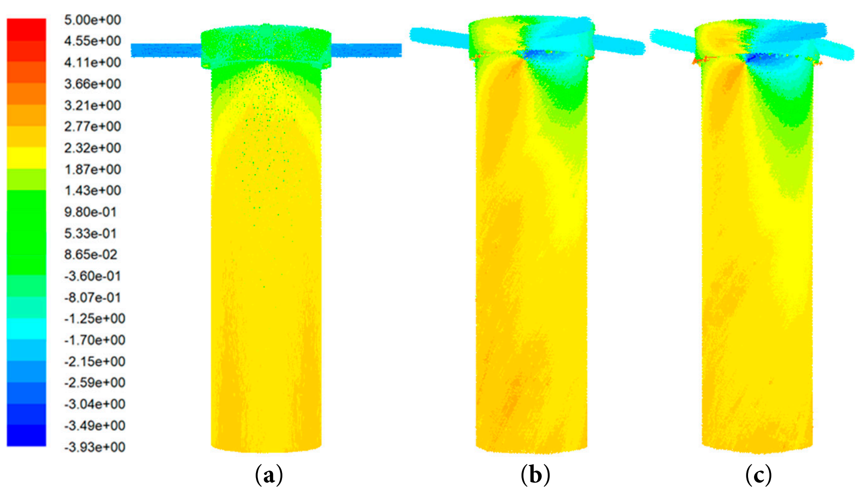

Figure 6: Wall velocity vector. (**a**) 0°; (**b**) 45°; (**c**) 60°.

Figs. 5 and 6 illustrate the liquid film velocity vectors, representing the velocity vectors at the cross-section and on the wall surface, respectively. The analysis is conducted from three aspects: vortex morphology, velocity distribution and liquid film characteristics.

1. 0°: Vortex morphology: There is no apparent swirling flow. The vectors are aligned neatly along the axial direction. Only minor fluctuations due to turbulence occur near the wall, with no curling vortices.

Velocity distribution: The velocity profile is parabolic, with a uniform velocity gradient. No secondary velocity peaks induced by swirl are observed.

Liquid film characteristics: The liquid film is uniformly distributed along the wall, maintaining consistent thickness. There is no film shifting or wrinkling caused by swirl, resulting in more stable flow but weaker mixing capability.

2. 45°: Vortex morphology: Small-scale vortices appear at the top swirl inlet. Near the tube wall, vectors exhibit the spiraling secondary flow.

Velocity distribution: The axial velocity is high at the tube center, with a large velocity gradient near the wall. The coupling of swirl and axial flow forms the composite "spiral + axial" flow pattern.

Liquid film characteristics: Due to centrifugal force from the swirling flow, the wall liquid film tends to be "thicker at the edges and thinner at the center". At the top inlet, the film exhibits slight wrinkling.

3. 60°: Vortex morphology: The vortices at the top are more intense, secondary flow near the wall is enhanced, and localized large vortices appear at the bottom of the tube, indicating stronger dominance of swirling flow compared to 45°.

Velocity distribution: The axial velocity at the center remains high, but the velocity gradient near the wall increases further. The velocity profile, shaped by the swirl.

Liquid film characteristics: The stronger centrifugal force makes the "thick edges, thin center" trend of the liquid film more pronounced. Wrinkling at the top inlet becomes more severe, and there is the risk of local film thinning/dry-out.

The specific comprehensive analysis of the effect swirl angle on vortex structure is compared in Table 2.

Table 2: Comparative analysis of the swirl angle on vortex structure.

Comparison Dimension	0° Swirl	45° Swirl	60° Swirl
Vortex strength	Weak (only minor turbulent fluctuations)	Moderate (small vortices at top + wall secondary flow)	Strong (large vortices at top + localized vortices at bottom)
Liquid film uniformity	Uniform distribution	Thick edges, thin center	Thicker edges, thinner center
Velocity profile	Purely axial (parabolic profile)	Axial-dominated + swirl correction	Axial + swirl-dominated
Mixing capability	Weak (pure axial flow, poor mixing)	Moderate (swirl enhance radial mixing)	Strong (enhanced radial mixing due to strong swirl)

The turbulence of the swirl angle on turbulent kinetic energy and dissipation rate is analyzed and compared, with the specific results shown in Fig. 7.

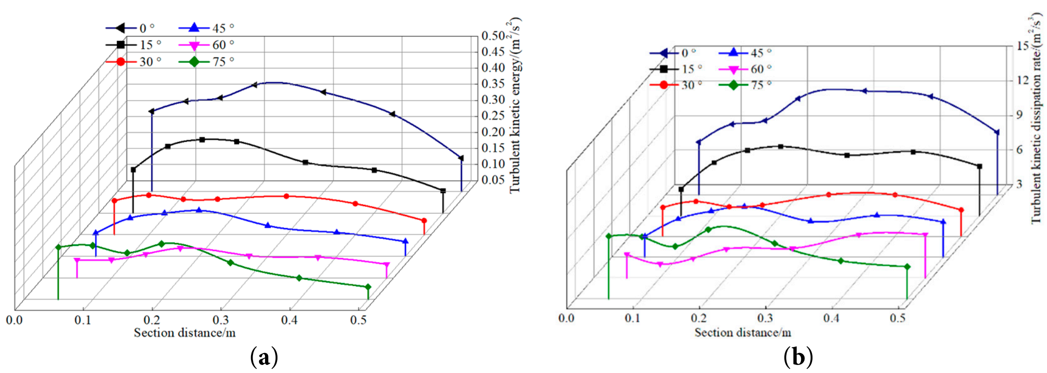

Figure 7: Swirl angle turbulence parameters. (**a**) Turbulent kinetic energy; (**b**) Turbulent kinetic dissipation rate.

Fig. 7 indicates the turbulent kinetic energy and dissipation rate at the tube wall cross-section for swirl angles of 15°~60°. Originating from flow velocity pulsation, turbulent kinetic energy refers to the dynamic energy carried by fluid micro-elements. Turbulent kinetic energy dissipation rate describes the rate at which turbulent kinetic energy is converted into internal energy through fluid motion. Fig. 7a depicts how turbulent kinetic energy changes along the flow path. From the change in turbulent kinetic energy in Fig. 7a, it can be seen that as the swirl angle increases, the turbulent kinetic energy of the liquid film at the tube wall first decreases and then increases. The non-monotonic variation of turbulent kinetic energy is attributed to the competition between flow regularization, which at moderate swirl intensities and the enhanced shear instability and vortex breakdown at high swirl intensities. The reason is: initial non-swirling flow is typically unstable, prone to generating disorganized small-scale turbulence. The introduction of swirling flow forces the liquid film to undergo ordered rigid-body rotation, forming the stable quasi-forced vortex. This large-scale ordered rotation suppresses small-scale random turbulent fluctuations, thereby reducing turbulent kinetic energy. After further increasing the swirl angle, shear forces and vortex breakdown dominate. The high rotational velocity creates a significant velocity difference between the center and the near-wall region, generating substantial turbulent kinetic energy. High-angle swirling flow tends to induce central recirculation or helical breakdown, and secondary flow intensifies. The liquid film experiences intense collisions and friction, shortening the energy dissipation path and increasing turbulent kinetic energy.

Fig. 7b reflects the variation curve of the turbulent dissipation rate. Consistent with the evolution law of turbulent kinetic energy, the dissipation rate demonstrates a non-monotonic distribution characteristic. In the initial non-swirling flow, the turbulence is isotropic. As swirl is introduced, the liquid film undergoes rigid-body rotation, and the film's large-scale ordered motion reduces frictional dissipation, causing the dissipation rate to decrease. When the swirl angle becomes excessively large, the extremely high velocity difference generates substantial shear stress. High-intensity vortex breakdown and intense secondary flow accelerate the energy cascade from large vortices to dissipative scales, leading to an increase in the dissipation rate. The correctness of the calculation is verified using the skin friction coefficient, and the wall friction coefficient results are shown in Fig. 8.

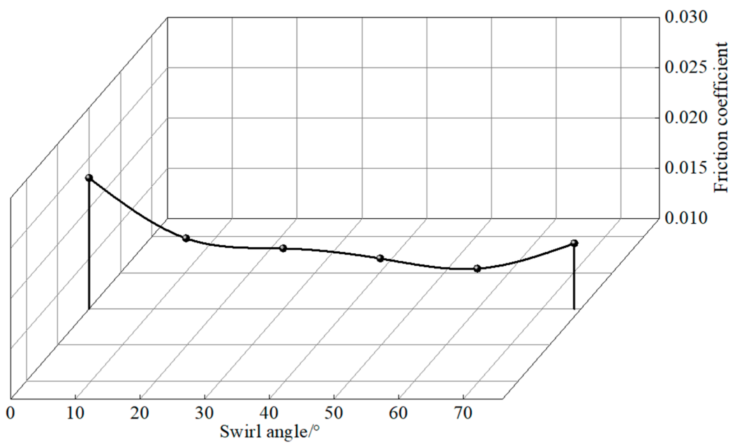

Figure 8: Wall friction coefficient.

Fig. 8 presents the analysis results of the wall friction coefficient. The ratio of the wall friction coefficient for non-swirling flow to that for swirling flow ranges from 1.35~1.64, which is consistent with the findings in reference [29]. This confirms the validity of the calculation in this research. Based on the analysis of data curves such as the liquid film thickness distribution, liquid film flow velocity, and changes in turbulence parameters, the falling film flow process with a swirl angle of 60° is most suitable. This is because the liquid film with a swirl angle of 60° has the smallest thickness and the most stable flow. Uniform and thin liquid film flow is most conducive to the heat transfer process between gas-liquid phases.

3.2 Influence of Platform Height on Falling Film

Supported by published research conclusions, the height of the built-in tube platform significantly influences the flow distribution of vertical falling liquid film, which acts as an essential influencing factor. Therefore, based on the research of 60° swirl angle, the platform height is analyzed and studied:

The impacts of platform height on the flow distribution of swirling falling liquid film are presented in Fig. 9, involving the spatial distribution of film thickness, flow velocity and turbulence intensity. According to Fig. 9a, a modest rise in liquid film thickness occurs near the inlet. In contrast, the liquid film thickness gradually decreases in both the fully developed area and the outlet region. The swirling liquid film possesses circumferential velocity and generates centrifugal force, facilitating significant circumferential expansion of liquid layer and thinning the liquid film in the axial direction. Height platform height corresponds to slightly thicker liquid film in the developing flow region. Under the platform height of 30 mm, the average liquid film thickness is 4.28 mm.

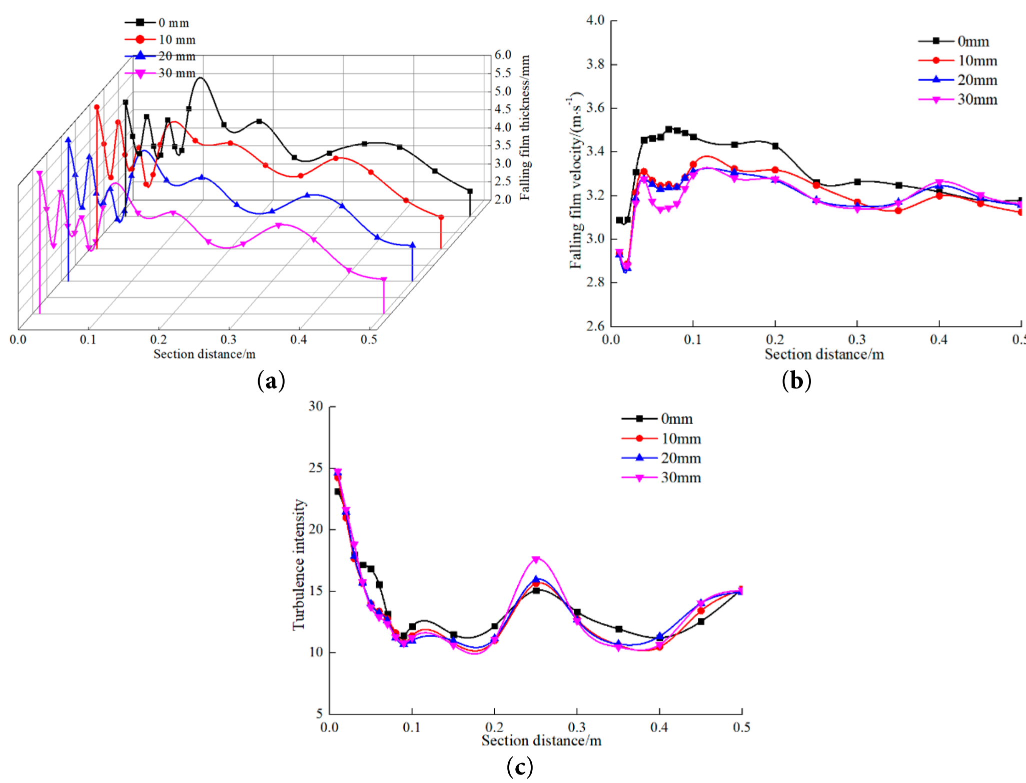

Figure 9: Influence of platform height on falling film. (**a**) Falling film thickness; (**b**) Falling film velocity; (**c**) Turbulence intensity.

Fig. 9b indicates the platform height effect on liquid film velocity. In contrast to straight opposed falling film flow, swirling liquid film feature tangential velocity, contributing to an obvious velocity elevation at the inlet region. Afterward, liquid film velocity in the development section is in fluctuating state, which is the stable liquid film fluctuation due to the swirling effect and wall shear force. The swirling falling film velocity at the inlet section is higher than at the opposed type, which is conducive to promoting heat transfer process between gas-liquid phases.

The axial distribution rules of liquid film turbulence intensity are illustrated in Fig. 9c. The turbulence intensity exhibits the gradual decreasing trend at the inlet, followed by sustained fluctuating variations in the flow development section. The higher platform height corresponds to stronger liquid film turbulence, which verifies that the platform structure contributes to the formation of an excellent liquid film flow state. It can be summarized from the above results that the arranged platform structure optimizes the liquid film distribution morphology and further enhances the gas-liquid heat transfer efficiency in swirling falling film systems.

3.3 Influence of Slot Width on Falling Film

Following distribution from the scrubbing cooling ring, the liquid film runs downward along the cooling tube within the slot channel. It follows that the slot width significantly dominates the morphological distribution of swirling falling liquid film. So in order to investigate the effect of slot width on vortex shedding film, the slot width of 2~5 mm is set to ensure the swirl angle of 60°, platform height is 30 mm, and *Re* remained constant. This results are indicated in Fig. 10.

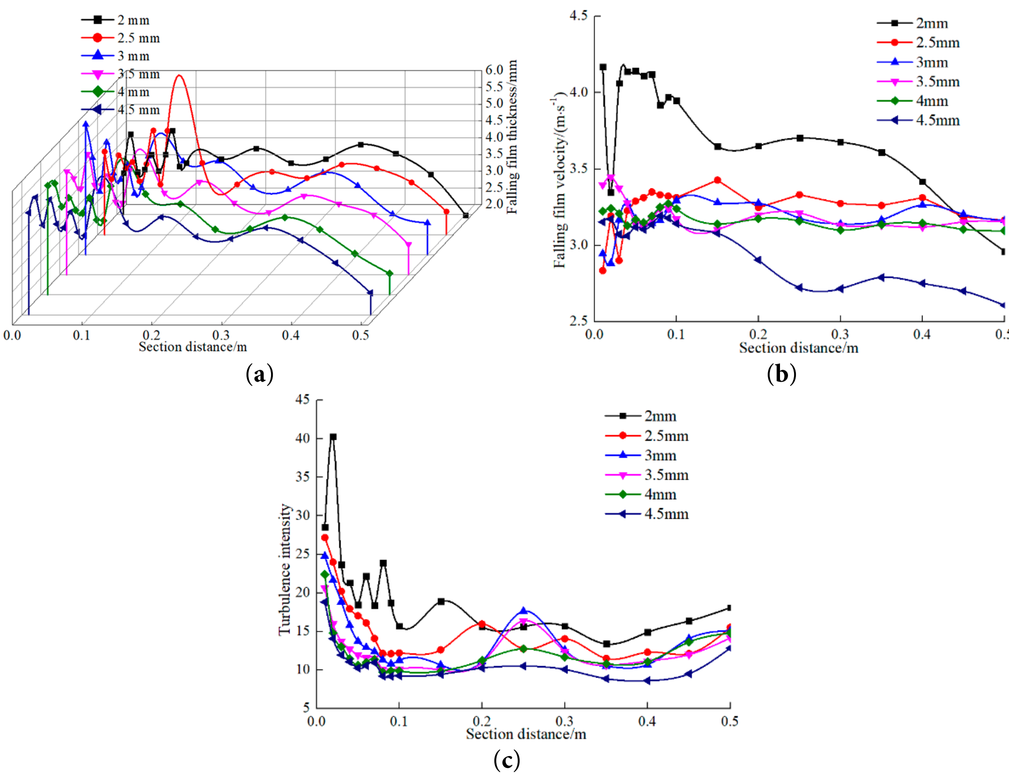

Figure 10: Influence of slot width on falling film. (**a**) Falling film thickness; (**b**) Falling film velocity; (**c**) Turbulence intensity.

Fig. 10a represents the effect of slot width on swirling film flow. The curves demonstrate that a wider slot contributes to enhanced surface fluctuation of liquid film, whose fluctuation amplitude is higher than that obtained from the opposed falling film model. When the slot width is less than 3 mm, the liquid film thickness is small, but the turbulence intensity is high. When the slot width is greater than 4 mm, the liquid film jet effect at the outlet decreases and liquid film fluctuation degree decreases. When the slot width is

3.5 mm, these two effects reach equilibrium: the liquid film is thick enough to avoid rupture, while thin enough to maintain an appropriate flow rate and mixing capacity, thus most conducive to forming the uniform liquid film.

Fig. 10b,c represent the influence of slot width on the liquid film flow velocity and turbulence intensity distribution. The curves reveal that the enlargement of slot width results in a continuous reduction of liquid film velocity near the inlet. This reason for this occurrence is that as the slot width increases, the jet effect of the liquid film at the outlet decreases, and the liquid film centrifugal force in the axial direction increases. The decrease in turbulence intensity indicates that the increase in slot width will reduce the degree of surface fluctuation of the liquid film.

3.4 Influence of Liquid Film Re on Falling Film

According to reference [41], the liquid film inlet *Re* has significant impact on the liquid film thickness distribution: the liquid film average thickness increases with the liquid film *Re* increase. Therefore, in order to investigate the effect of liquid film *Re* on swirling falling film flow, the liquid film *Re* is set to 2.42×10^4~3.63×10^4, and the calculation is carried out under the condition that the swirl angle, platform height, and slot width remain unchanged. The results are indicated in Fig. 11.

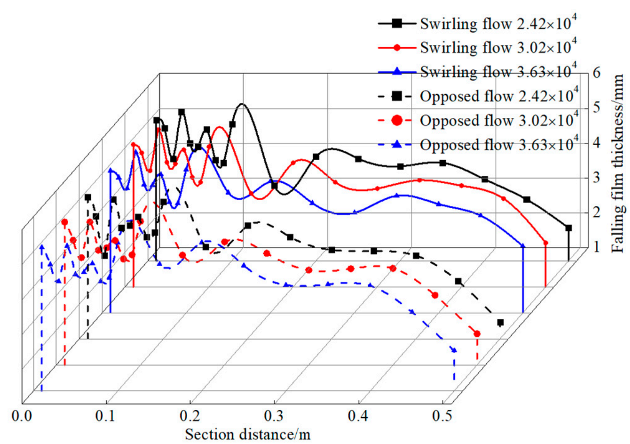

Figure 11: Influence of *Re* on falling film thickness distribution.

As shown in Fig. 11, regardless of whether it is opposed or swirl type, the average liquid film thickness at the axial distance increases with the increase of *Re*. The elevated *Re* contributes to higher liquid film velocity, leading to an increase in the falling liquid film thickness. The liquid film thickness in the inlet section of the two types of falling film changes significantly and shows an overall upward trend, which is consistent with the principle of mass conservation. Liquid film thickness gradually decreases in the development and export stages. This result is consistent with the research findings in reference [41], which is due to the large fluctuations of the liquid film in the inlet part of the accumulation, while the fluctuations of the liquid film in the developing and outlet parts are relatively small. Gravity accelerates the flow of liquid along the axial direction, stretching the liquid film and thinning it. At higher *Re*, the thickness reduction is more pronounced due to the greater inertial force. Under identical *Re* conditions, the swirling falling film exhibits a larger average liquid film thickness at the inlet section compared with the conventional opposed falling film. In contrast, smaller film thickness values are observed in the developing and outlet regions. This phenomenon arises because the swirling motion induces intense velocity fluctuations in the circumferential direction, thickening the liquid film at the inlet. Accordingly, the swirling effect dose not merely increase the overall liquid film thickness. It redistributes the liquid holdup along the axial direction of the cooling tube.

4 Investigation on Gas-Liquid Two-Phase Heat Transfer Behavior

4.1 Effect of Liquid Film Temperature on Thermal Heat Transfer Characteristics

For swirling falling film systems, heat and mass transfer occur when high-temperature gas interacts with the cooling liquid film triggering interfacial evaporation and phase change. The liquid film inlet section is the most intense part of gas-liquid two-phase heat transfer, and liquid film initial temperature directly affects heat transfer effect between the gas-liquid phases. Before studying heat transfer between gas and liquid phases, corresponding assumptions need to be made for the model. The specific assumptions are as follows:

1. The thermophysical parameters of both gas and liquid phase are independent of temperature variation.
2. The initial flow parameters of two-phase maintain constant during the whole heat and mass transfer process.
3. Convective heat transfer exists between the gas inside the tube and the wall surface, while radiative heat transfer is neglected. The wall condition is a constant wall temperature.
4. The gas phase is an incompressible gas, ignoring surface dissolution of the gas.

In the numerical simulation of gas-liquid two-phase heat transfer, the Energy equation is activated, and the Rosseland radiation model is adopted to describe two-phase interfacial interaction. This model is selected primarily because the gas-liquid mixture inside the tube can be regarded as a transparent medium. As reported in previous studies [40], the Rosseland mode provides numerical results that are in good agreement with experimental data. Compared with the DO radiation model, the Rosseland method effectively reduces the computational cost while ensuring satisfactory stability and calculation accuracy, making it more suitable for the present numerical simulation. The simulated phase transition at the gas-liquid interface adopts the Lee model, and the basic principle is that there is heat transfer temperature difference driving force between gas-liquid phases, and the mass is transferred from liquid phase to gas phase through the source term. The evaporation intensity is defined using the Lee model.

The boundary conditions of the gas-liquid interface are captured by the VOF method to capture the diffusion interface, taking into account the surface tension between the gas-liquid phases. The CSF model is used without considering the thermal capillary effect. The gas phase is an incompressible gas because the flow velocity in the calculation area is much lower than 0.3 Ma, and the main thermal resistance exists on the liquid film side. Compared with buoyancy, change in gas density only impose a minor influence on the overall flow characteristics. Therefore, an incompressible gas is used to define the calculation density. Complex gas mixtures are crucial because the evaporation of pure vapor is only driven by thermodynamic temperature differences, while in the mixture, evaporation is also controlled by the concentration difference of vapor on the gas phase side. When using the Lee model, the saturation temperature T_{sat} is adjusted so that evaporation intensity is influenced by the combined effects of mass and heat transfer at the gas-liquid interface. When liquid film at the wall is in uniform flow, it can satisfy the phase change heat transfer process between gas and liquid phases, and there will be no dry spots on the wall. The conservation of mass in the liquid phase is controlled by monitoring the difference in liquid phase mass flow rate between the inlet and outlet, and comparing it with the mass reduction by evaporation. In this research, the focus is on direct contact heat transfer between gas and liquid phases inside the tube, without involving external thermal resistance and heat transfer.

Gas-liquid two-phases undergoes phase change heat transfer inside tube, with energy source term and mass source term customized using UDF. VOF media are divided into five types: water, air, syngas (H_2, CO), and vapor. This is because at the beginning of heat transfer in gas-liquid two-phase flow, there are two media in the tube: water and air. When high-temperature synthesis gas enters the tube and undergoes phase change heat transfer with the liquid film, the liquid film evaporates into vapor, so these five media need to be set in the VOF medium settings. Compared with simple air-vapor systems, the presence of syngas can alter the thermophysical properties of the gas phase, including density, viscosity, thermal conductivity, thereby affecting the shear stress and heat transfer coefficient at the gas-liquid interface. In actual engineering conditions, the gaseous medium presents complex components composed of air and synthesis gas. Before the simulation calculation, the simulation method for the heat transfer process is first validated. Experimental data selected from reference [42], the simulation verification results are shown in Fig. 12.

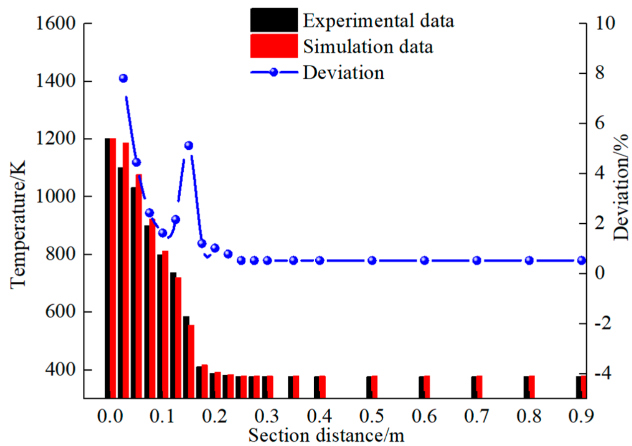

Figure 12: Comparison between simulation calculation and experimental data verification.

Fig. 12 presents the comparative analysis and validation results between simulation calculations and experimental data. As shown in Fig. 12, the deviation between simulated calculation data and experimental measurement values is very small, which proves the feasibility and accuracy of the simulation calculation method. Therefore, this simulation approach is adopted in the research. A series of controlled simulations with liquid film temperatures ranging from 288 K to 318 K are conducted to clarify its regulatory effect on gas-liquid heat transfer behavior. The relevant numerical outcomes are visualized in Fig. 13.

Fig. 13a compares the cross-sectional temperature distributions between conventional opposed falling film and swirling falling film flow. The cross-sectional distance of the horizontal axis is the axial distance inside the pipe. As the axial distance increases, the average cross-sectional temperature decreases. With the elevation of liquid film temperature, the average cross-sectional temperature rises accordingly. This phenomenon occurs because an increase in liquid film temperature reduces the gas-liquid heat transfer temperature difference, which weakens the thermal driving potential and further lower the overall gas-liquid heat transfer efficiency. By comparing the cross-sectional temperatures of two falling film methods, the relative temperature of the inlet section is higher, while the swirling cross-section temperature in the unfolding and outlet sections is higher. This difference stems from the notable tangential velocity component within the liquid film, which enables the liiquid to flow downward along the tube wall in the spiral trajectory. Tangential flow increases the contact area and frequency between the liquid film and high-temperature gas, introduces forced convection disturbance at the interface, and generates significant secondary flow and local vortex structures near the wall. And due to the thinner thickness of the swirling liquid film, which has a smaller thermal resistance, enhancing the heat transfer effect between gas-liquid phase, resulting in a faster temperature drop at the cross-section. In the development stage, the tangential velocity further decreases, the strengthening effect of swirl on gas-liquid two-phase heat transfer weakens, gas-liquid temperature difference decreases, and the heat transfer driving force decreases, so the decrease in cross-sectional temperature is slower.

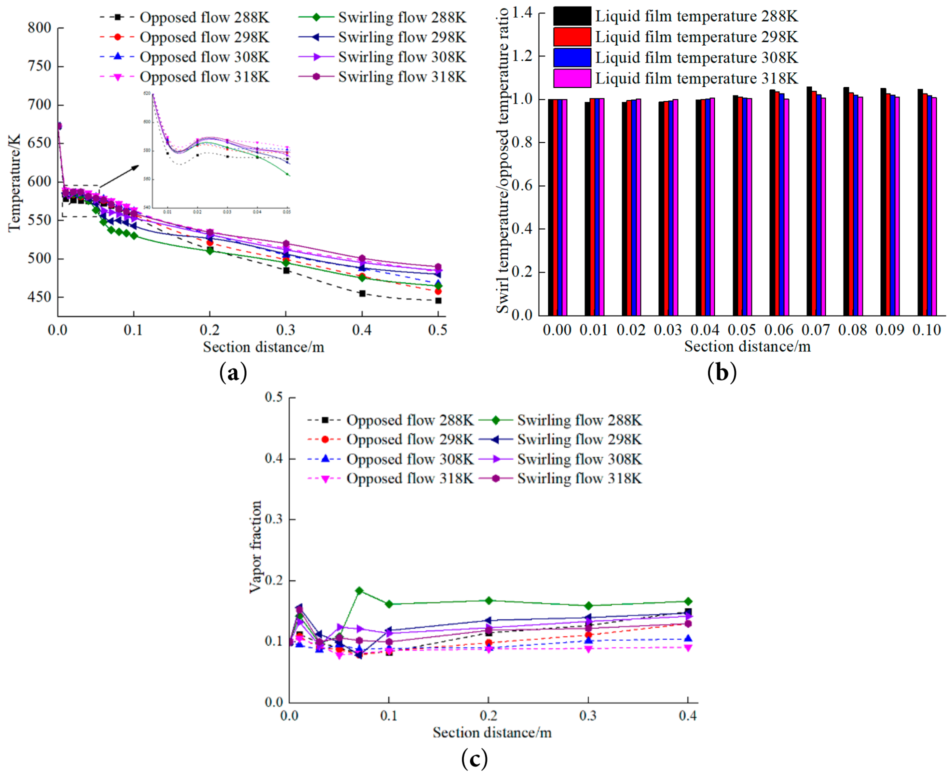

Figure 13: Influence of liquid film temperature on heat transfer. (**a**) Section temperature; (**b**) Ratio of swirl temperature to opposed temperature; (**c**) Section vapor fraction.

Fig. 13b shows the ratio of swirl section temperature to opposed section temperature (section distance 0~0.1 m). The bar chart quantitatively characterizes the temperature discrepancy between swirling and opposed falling film sections. As reflected by the variation trend of the temperature ratio in the figure, under low liquid film temperature conditions, the swirling structure exhibits a more significant temperature rise along the axial direction compared with the opposed structure, with the temperature ratio gradually exceeding 1. In contrast, the continuous increase in the bulk liquid film temperature leads to the gradual reduction in the cross-sectional temperature ratio between the two flow models. This phenomenon demonstrates that, at the liquid film inlet region, low-temperature liquid film conditions correspond to the more intense temperature variation in the swirling falling film system, which enhances the gas–liquid two-phase heat transfer intensity.

Fig. 13c reflects the cross-sectional vapor volume fraction variation curves for two types of falling film methods. From the curve data in Fig. 13c at the inlet section, the vapor volume fraction in the swirling type is relatively high, indicating a larger amount of liquid film evaporation. This is because falling film has circumferential velocity in the inlet section of swirling type, which results in more sufficient contact between liquid film and high-temperature gas, leading to a higher film evaporation rate compared to the opposed type. In the two types of falling film methods, the liquid film evaporation rate in the inlet section is in a fluctuating state, as the liquid film thickness and falling film flow rate at the inlet section are both fluctuating, resulting in the inability to maintain a constant increase in liquid film evaporation rate. As the axial distance increases, the cross-sectional vapor volume fraction of the two falling film methods is basically on an increasing trend. The trend of changes in vapor content is consistent with reference [40]. This indicates that the evaporation of the cooling liquid film in the latter half of the cooling tube is relatively high. By comparing the cross-sectional temperature and vapor volume fraction in Fig. 13, it was found that heat transfer effect between the liquid film and high-temperature gas is best when the liquid film temperature is at a lower temperature. And due to the circumferential velocity distribution of swirl type falling film, the heat transfer effect of the swirling type falling film is better at the inlet section where gas-liquid two-phase heat transfer is most intense.

Heat transfer coefficient (HTC) is the standard for characterizing the heat transfer strength between gas and liquid phases, and the HTC relationship as follows [7]:

$$h = \frac{\Delta H m_g}{A \Delta t_m} \tag{13}$$

h is gas-liquid two phase HTC, W/(m^2·K), ΔH is gas-phase enthalpy change, J, m_g is gas phase mass flow rate, kg/s, A is Gas liquid two-phase heat transfer area, m^2, Δt_m is logarithmic mean temperature difference, K.

To characterize the heat transfer capability between gas-liquid two-phase systems, the dimensionless parameter h^+ is introduced. The calculation formula for h^+ is as reference [7]:

$$h^+ = h\left(\frac{{\mu_l}^2}{{\rho_l}^2 {\lambda_l}^3 g}\right)^{\frac{1}{3}} \tag{14}$$

h^+ is dimensionless parameter, ρ_l is liquid film density, kg/m^3, λ_l is liquid film thermal conductivity, W/(m·K), g is gravity acceleration, m/s^2.

Introducing the dimensionless parameter T_D [7] as the ratio of gas phase to liquid phase, the specific calculation formula is as follows [7]:

$$T_D = \frac{T_g}{T_l} \tag{15}$$

T_D is dimensionless temperature parameter, T_g is gas temperature, K, T_l is liquid film temperature, K.

Fig. 14a illustrates the influence of liquid film temperature on the gas–liquid two-phase heat transfer coefficient (HTC). The HTC declines as the liquid film temperature rises, and the HTC gap at identical cross-sections becomes narrower accordingly. This can be attributed to the larger temperature difference between the liquid film and gas phase under low liquid film temperature conditions, which intensifies gas–liquid heat exchange and yields a higher HTC. Along the axial direction, the HTC rises with increasing cross-sectional distance, whereas its growth rate diminishes. The maximum HTC reaches roughly 700 W/m^2·K.

Fig. 14b presents the variation of h^+ curves under various gas-liquid temperature ratios. The dimensionless temperature T_D, representing the gas-liquid temperature ratio, shows the positive correlation with h^+, where h^+ rises with increasing T_D. This trend reveals that the larger temperature difference between the liquid and gas phases supplies greater driving potential for interfacial heat exchange, thereby achieving enhanced gas-liquid heat transfer performance.

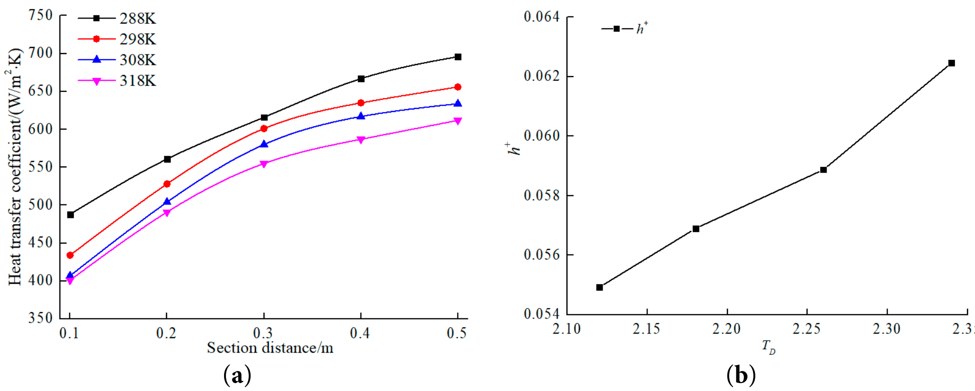

Figure 14: HTC of liquid film temperature and fitting curve of h^+. (**a**) HTC of liquid film temperature; (**b**) Fitting curve of h^+.

4.2 Effect of Liquid Film Re on Thermal Heat Transfer Characteristics

The effects of liquid film temperature on falling film heat transfer performance have been analyzed in Section 4.1. Comparative results confirm that low-temperature cooling liquid films can effectively strengthen the gas–liquid two-phase heat transfer, and the swirling falling film exhibits superior heat transfer capability at the inlet section. In addition to temperature, the liquid film *Re* is another critical parameter dominating gas–liquid heat transfer characteristics, especially at the inlet region where the two-phase heat exchange is the most intense. To further explore the influence of liquid film *Re* on the heat transfer behavior inside the scrubbing cooling tube, numerical simulations are performed at the constant liquid film temperature of 288 K, with the liquid film *Re* varying from 2.42×10^4 to 3.63×10^4. The corresponding research results are demonstrated in Fig. 15.

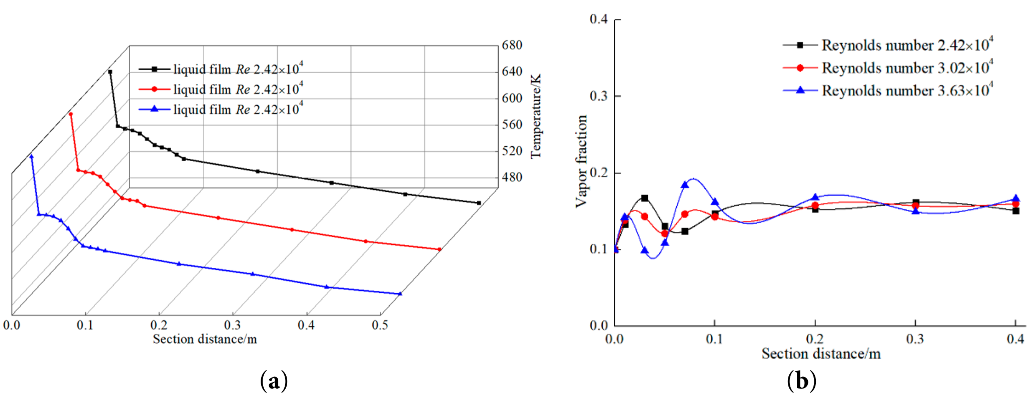

Figure 15: Influence of liquid film Reynolds number on heat transfer. (**a**) Section temperature; (**b**) Section vapor fraction.

Fig. 15a indicates the cross-sectional liquid film average temperature under different liquid film *Re* conditions. The horizontal axis represents the axial distance inside the tube. As shown in the data curve in Fig. 15a, liquid film temperature decreases the fastest in the inlet section, while the temperature decreases more steadily in the development and outlet sections. This can be explained by the drastic variation of liquid film thickness in the inlet region, which enlarges the gas-liquid contact area and facilitates sufficient heat exchange. As the liquid film *Re* rises, the average cross-sectional temperature gradually declines. Increasing liquid film *Re* accelerates the flow velocity of the liquid film, enabling the liquid phase to carry more heat away and lowering the average cross-sectional liquid film temperature. The temperature at the outlet reaches approximately 470 K.

Fig. 15b illustrates the evolution of vapor volume fraction on different cross-sections. Consistent with the trend shown in Fig. 13b, obvious variations of vapor content occur within the inlet region, whereas the developing and outlet sections maintain the relatively steady state. The vapor volume fraction rises along the axial direction, and such variation corresponds to the liquid film temperature distribution on each cross-section. The higher liquid film *Re* contributes to elevated vapor content, which further intensifies interfacial heat transfer between gas and liquid phases.

Fig. 16a shows the liquid film *Re* effect on gas-liquid two-phase HTC. HTC increases with liquid film *Re* increase, and the difference in HTC at the same cross-section also increases. The reason is that when the liquid film *Re* is at the smaller value, the liquid film flow velocity is slower and the heat exchange ability with gas phase is lower. The higher liquid film *Re* corresponds to an accelerated liquid film flow velocity, which strengthens the heat exchange capacity with the gas phase and leads to the gradual rise in the HTC. HTC increases with cross-sectional distance increase, but the increase magnitude gradually decreases.

Fig. 16b indicates the h^+ calculation data and fitting curves for different liquid film *Re*. From the fitting formula in Fig. 16b, h^+ is directly proportional to the liquid film *Re*, but the increase in h^+ gradually decreases. This trend reveals that once the *Re* rises above the specific threshold, further increasing *Re* exerts only the marginal influence on gas–liquid interfacial heat transfer process. The fitting curve R^2 is 0.999.

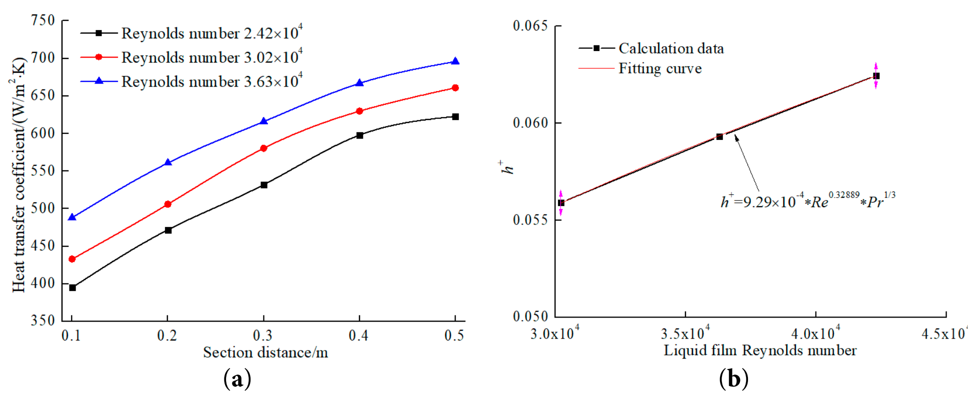

Figure 16: HTC of liquid film *Re* and fitting curve. (**a**) HTC of liquid film *Re*; (**b**) h^+ fitting curve.

5 Conclusions and Prospects

5.1 Conclusions

This study adopts refined numerical methods to explore the gas-liquid two-phase flow features and thermal performance of vertically falling swirling films operating at high *Re*. Through the visualization of the velocity vector, vortex structure (turbulent criterion) and temperature field, the mechanism of swirling structure on liquid film distribution and heat transfer performance is systematically revealed. The influences of swirl angle, platform height, and slot width to cooling liquid film deposition process of swirl is studied. And analysis liquid film temperature and *Re* influences on gas-liquid two-phase heat transfer process. Conclusions obtained after the research are as follows:

1. The swirl angle affects liquid film thickness, velocity, and turbulence intensity distributions in the inlet and development sections. As the swirl angle increases, the liquid film thickness gradually decreases, the liquid film flow velocity gradually increases, and the turbulence intensity gradually stabilizes. When the swirl angle is 60°, the average liquid film thickness is 4.03 mm, the liquid film is at its

minimum value, minimizing heat transfer resistance to the greatest extent possible and the surface fluctuation of the liquid film is the most stable.

2. The platform height increases leads to average liquid film thickness increase. When the platform height is 30 mm, the average liquid film thickness is 4.28 mm. The platform height increase also stabilizes liquid film flow, and a height of 30 mm is the optimal height.
3. The cooling ring slot creates the jet effect on liquid film at liquid film outlet, and the slot width increases leads to the average liquid film thickness increases. The liquid film velocity gradually decreases, and turbulence intensity gradually stabilizes. When the slot width is 3.5 mm, the liquid film thickness, velocity, and turbulence intensity are the optimal values.
4. The cross-section average temperature decreases with axial distance increases, with the greater decrease in inlet section cross-section average temperature. Vapor volume fraction in the inlet section fluctuates and increases with the axial distance increase. The swirl type falling film heat transfer has the better gas-liquid two-phase heat transfer effect in inlet section than opposed type. Both low-temperature cooling liquid film and high *Re* are beneficial for enhancing the heat transfer effect between the gas and liquid phases. The maximum HTC is approximately 700 $W/m^2 \cdot K$. Fitting curves can effectively predict the trend of gas-liquid heat transfer.

5.2 Prospects

Based on numerical calculations and in-depth mechanistic investigations of vortex falling films and gas-liquid two-phase heat transfer, this work proposes the following prospects for subsequent research:

1. Conduct experimental verification in future work to quantitatively analyze flow and heat transfer process of swirling falling film.
2. In future research, consider the convective heat transfer between the wall and the external environment, and further improve the study of gas-liquid two-phase heat transfer inside tube.

Acknowledgement: This work was supported by the Henan Provincial Natural Science Foundation General Project.

Funding Statement: Henan Provincial Natural Science Foundation General Project (252300421902).

Author Contributions: Lishuang Zheng: conceptualization, data curation, formal analysis, investigation, methodology, project administration, validation, writing—original draft, writing—review & editing. Fengjun Chen: Formal analysis, software, visualization, writing—review & editing. All authors reviewed and approved the final version of the manuscript.

Availability of Data and Materials: All the data in this article are true and available.

Ethics Approval: Not applicable.

Conflicts of Interest: The authors declare no conflicts of interest.

References

1. Chen X, Sun J, Yu K, Wu J, Yin J. Design of novel bracket structure for falling film devolatilizer and numerical simulation of its film-forming property. Chem Eng J. 2024;499:156317. [CrossRef].
2. Byun S, Lee S, Baek C, Kim J, Kim Y. Impact of distributor design variables on heat transfer characteristics in falling film evaporators using water. Int Commun Heat Mass Transf. 2024;159:108312. [CrossRef].
3. Azimifar M, Moradian A, Jafarian A. A numerical investigation on the dynamics of particle deposition and fouling on a vertical falling film pipe. J Water Process Eng. 2024;66:105990. [CrossRef].

4. Mascarenhas N, Mudawar I. Investigation of eddy diffusivity and heat transfer coefficient for free-falling turbulent liquid films subjected to sensible heating. Int J Heat Mass Transf. 2013;64:647–60. [CrossRef].
5. Syafei MH, Siswantara AI, Budiyanto MA, Syah I, Rizianiza I, Septiyana A. Three-dimensional CFD analysis of palm-based oil falling films: Tangential velocity and hydrodynamic instabilities on vertical tubes. Int J Heat Fluid Flow. 2026;119:110326. [CrossRef].
6. Zhao Y, Markides CN, Matar OK, Hewitt GF. Disturbance wave development in two-phase gas–liquid upwards vertical annular flow. Int J Multiph Flow. 2013;55:111–29. [CrossRef].
7. Wang L. Research on phase change of vertical annular falling film heat transfer in tube at high liquid film Reynolds number. Int J Heat Mass Transf. 2026;255:127820. [CrossRef].
8. Lin Y, Zhang G, Yi Z, Cong M, Shen H, Zhao J. Experimental study and CFD simulation on the falling film characteristics of viscous fluid outside a vertical tube at very low Reynolds numbers. Chem Eng Res Des. 2025;216:174–85. [CrossRef].
9. Cao G, Min X, Xi W, Wu S, Zhang S, Liu G, et al. Experimental study of the flow dynamics and thermodynamic properties of a tube in vertical falling film evaporator for data center cabinets. Case Stud Therm Eng. 2023;50:103436. [CrossRef].
10. Xue T, Ruan F, Wang Z. Investigation on wave morphology and temperature distribution of falling liquid film in a vertical tube. Flow Meas Instrum. 2023;90:102325. [CrossRef].
11. Yan L, Wang Y, Wu Z, Dai Z, Yu G, Wang F. Research of vertical falling film behavior in scrubbing-cooling tube. Chem Eng Res Des. 2017;117:627–36. [CrossRef].
12. Pan C, Huang S, Qiu Y, Li S, Jia T, Li Y, et al. A new type of absorber based on ultrasonic atomization enhanced in-tube falling film absorption process. Int J Refrig. 2026;183:81–94. [CrossRef].
13. Cheng Q, Song X, Dang YX, Du S, Liu ZB, Li MJ. Analysis and improvement of full field falling film and heat transfer characteristics in the evaporators. Appl Therm Eng. 2026;289:129964. [CrossRef].
14. Liang H, Hu Z, Tian Q, Lu C, Yu H, Cao X, et al. Investigation of external heat transfer characteristics in a partially submerged vertical heat exchanger tube bundle. Nucl Eng Des. 2025;442:114234. [CrossRef].
15. Zhang H, He Y, Liu J, Zhou Y. Experimental assessment on heat transfer characteristics of falling-film evaporation under mutual parameters' coupling between circular and half-oval tubes. Therm Sci Eng Prog. 2025;67:104092. [CrossRef].
16. Hasan AH, Mohammed SK, Hewakandamby B, Azzopardi B. Experimental study of the three-dimensional interfacial wave structure of freely falling liquid film in a vertical large pipe diameter. Chem Eng Res Des. 2021;169:66–76. [CrossRef].
17. Wang W, Liao Y, Yan Y, Zhao B, Wang T, Shangguan S. Numerical study on falling film flowing characteristics of R113 inside vertical tube under different structural conditions. Chin J Chem Eng. 2020;28(1):23–32. [CrossRef].
18. Azimibavil S, Jafarian A, Tizbin S, Mouza AA. A numerical investigation into a long tube falling film evaporator in a zero liquid discharge (ZLD) process. Chem Eng Sci. 2022;257:117701. [CrossRef].
19. Ma L, Ding Y, Zhu X, Wang H, Liao Q. Numerical investigation on falling film flow and heat transfer characteristics over corrugated plates. Int J Thermal Sci. 2024;198:108882. [CrossRef].
20. Vasques J, Cherdantsev A, Cherdantsev M, Isaenkov S, Hann D. Comparison of disturbance wave parameters with flow orientation in vertical annular gas-liquid flows in a small pipe. Exp Therm Fluid Sci. 2018;97:484–501. [CrossRef].
21. Aktershev SP, Alekseenko SV. New model for waves in a falling film. Procedia IUTAM. 2013;8:3–12. [CrossRef].
22. Ahmadi N, Rostami S, Damya A. Smart design of conical vortex generators for heat transfer enhancement: A synergy of CFD and Bio-inspired optimization. Results Eng. 2025;27:105613. [CrossRef].
23. Liu W, Xu G, Gu X, Yao J, Li M, Lei M, et al. Experimental analysis and thermodynamic modeling for multilevel heat exchange system with multifluid in aero engines. Energy. 2025;315:134373. [CrossRef].
24. Li C. Characteristics of the high-temperature water film evaporation with countercurrent turbulent air flow in the duct. Ann Nucl Energy. 2019;130:1–7. [CrossRef].
25. Rasouli E, Tano IN, Aboud A, Seo J, Lamprinakos N, Rollett A, et al. Experimental characterization of an additively manufactured heat exchanger for high temperature and pressure applications. Appl Therm Eng. 2025;264:125412. [CrossRef].

26. Cramer E, Ramadhan RS, Meyer T. Solution for the coupled heat and mass transfer in falling film absorption using partial discretization via orthogonal collocation. Chem Eng Res Des. 2025;224:420–32. [CrossRef].
27. Hu P, Du K, Zhai S, Yang Y. Experiment study of water film/air counter-current flow heat transfer on a vertical plate for passive containment cooling system. Nucl Eng Des. 2018;328:73–9. [CrossRef].
28. Jia B, Yang L, Politaeva N, Zhou J, Sadeghi K. Review on droplet falling film evaporation in desalination: A focus on heat transfer enhancement of micro-nano structured surfaces. Desalination. 2025;598:118373. [CrossRef].
29. Zeng J, Wang Y, Liu Q, Yu G, Wang F, Li P, et al. Velocity distribution and decay characteristics of the liquid film in falling swirling flow. Int J Heat Mass Transf. 2025;253:127624. [CrossRef].
30. Jin M, Liang F, Zheng W, Ding R, Wang S, Li C. Experimental investigation of swirler-induced liquid film spatiotemporal behavior in horizontal gas–liquid swirling flow. Sep Purif Technol. 2026;384:136107. [CrossRef].
31. Wan Z, Li Y. Refrigerant film flow and heat transfer characteristics on the elliptical tube under constant wall temperature. Appl Therm Eng. 2022;200:117669. [CrossRef].
32. Zhao CY, Yao ZL, Qi D, Ji WT, Li AG, Tao WQ. Numerical investigation of tube bundle arrangement effect on falling film fluid flow and heat transfer. Appl Therm Eng. 2022;201:117828. [CrossRef].
33. Zhu X, Haglind F. Computational fluid dynamics modeling of liquid–gas flow patterns and hydraulics in the cross-corrugated channel of a plate heat exchanger. Int J Multiph Flow. 2020;122:103163. [CrossRef].
34. Shen Y, Shi C, Zhang L, Bu S, Xu W, Zhang Z, et al. Falling film evaporation in a vertical tube with a new type of liquid distributor designed using the brachistochrone principle. Vacuum. 2021;187:110023. [CrossRef].
35. Kumar A, Hardik BK. Heat transfer distribution and pressure fluctuations during flow boiling in a pipe with different orientations. Appl Therm Eng. 2022;201:117822. [CrossRef].
36. Zhao L, Tang W, Wang L, Li W, Minkowycz WJ. Heat transfer and fouling characteristics during falling film evaporation in a vertical sintered tube. Int Commun Heat Mass Transf. 2019;109:104388. [CrossRef].
37. Cao Y, Nguyen PT, Jermsittiparsert K, Belmabrouk H, Alharbi SO, Khorasani MS. Thermal characteristics of air-water two-phase flow in a vertical annularly corrugated tube. J Energy Storage. 2020;31:101605. [CrossRef].
38. Dong X, Chen W, Cheng Q, Liu Y, Dai H. Numerical analysis of thermal-hydraulic characteristics of steam-air condensation in vertical sinusoidal corrugated tubes. Int J Heat Mass Transf. 2021;164:120558. [CrossRef].
39. Jiang J, Hu B, Wang RZ, Liu H, Zhang Z, Li H. A dynamic model for predicting condensation heat and mass transfer characteristics in falling film condenser. Int J Heat Mass Transf. 2021;176:121434. [CrossRef].
40. Yan LC. Study on vertical falling film flow and heat and mass transfer process in scrubbing cooling chamber [dissertation]. Shanghai, China: East China University of Science and Technology; 2017. (In Chinese).
41. Huang X, Wang Y, Wang L, Yu G, Wang F. Effect of structural optimization of scrubbing cooling rings on vertical falling film flow characteristics. ACS Omega. 2022;7(24):21291–305. [CrossRef].
42. Li T, Yuan ZL. Investigation on gas-liquid heat and mass transfer in vertical pipe of texaco gasifier quench chamber. J Northeast Electr Power Univ. 2013;33(3):47–51. (In Chinese). [CrossRef].